Phase-Controllable Spoof Surface Plasmon Coupling From Bull's Eye Aperture to Planar Silicon Waveguide in the Terahertz Band

Taiyu Okatani, Kaoru Imai, Yuma Takida, Seigo Ohno, Hiroaki Minamide, *Member, IEEE*, and Yoshiaki Kanamori, *Member, IEEE*

***Abstract*—We demonstrate spoof surface plasmon coupling of a terahertz wave propagating in free space into a planar silicon waveguide through a bull's eye structure with a subwavelength aperture. Spoof surface plasmon polaritons induced by the bull's eye structure on the backside of the substrate propagate to the frontside through the aperture and couple into the waveguide. Electromagnetic field simulations revealed that the spoof surface plasmon polaritons propagating to the frontside show directivity along the incident polarization direction, and that the phase can be controlled by placing a *Y*-branched silicon waveguide beside the aperture. A prototype device was fabricated by bonding a copper-plated substrate with a bull's eye aperture and a waveguide fabricated by silicon micromachining. A monochromatic wave of 0.42–0.49 THz from a backward terahertz-wave parametric oscillator was injected into the bull's eye structure, and the intensity of the emitted wave from the end of the waveguide was measured. Directional coupling into the waveguide was confirmed from the intensity change depending on the incident polarization direction when using a straight waveguide. In addition, the phase difference between the two ends of the *Y*-branched waveguide was confirmed by the intensity change showing constructive or destructive interference depending on the polarization direction. These results indicate that it is possible to couple an incident wave into a planar waveguide perpendicular to it by controlling the phase via spoof surface plasmon coupling, suggesting its applicability to new experimental and practical systems in the terahertz band, such as beyond 5G/6G communications.**

***Index Terms*—Bull's eye aperture, phase control, silicon waveguide, surface plasmon, terahertz.**

Manuscript received 19 March 2024; revised 9 April 2024; accepted 16 April 2024. Date of publication 22 April 2024; date of current version 5 July 2024. This work was supported by RIKEN–Tohoku University Science and Technology Hub Collaborative Research Program. *(Corresponding author: Taiyu Okatani.)*

Taiyu Okatani, Kaoru Imai, and Yoshiaki Kanamori are with the Department of Robotics, Graduate School of Engineering, Tohoku University, Sendai 980-8579, Japan (e-mail: taiyu.okatani.a3@tohoku.ac.jp; kaoru.imai.q4@dc.tohoku.ac.jp; ykanamori@tohoku.ac.jp).

Yuma Takida and Hiroaki Minamide are with the Tera-Photonics Research Team, RIKEN Center for Advanced Photonics, RIKEN, Sendai 980-0845, Japan (e-mail: yuma.takida@riken.jp; minamide@riken.jp).

Seigo Ohno is with the Department of Physics, Graduate School of Science, Tohoku University, Sendai 980-8578, Japan, and also with the Tera-Photonics Research Team, RIKEN Center for Advanced Photonics, RIKEN, Sendai 980-0845, Japan (e-mail: seigo@tohoku.ac.jp).

This article has supplementary material provided by the authors and color versions of one or more figures available at https://doi.org/10.1109/TTHZ.2024.3392157.

Digital Object Identifier 10.1109/TTHZ.2024.3392157

I. Introduction

TERAHERTZ waves in the frequency band from 0.1 to 10 THz are attracting attention as carrier waves for next-generation mobile communications called beyond 5G/6G [1], [2], [3]. Terahertz waves, which have shorter wavelengths than conventional radio waves and are closer to light waves, are difficult to pass through the shadows of obstacles. Furthermore, due to its large attenuation in the atmosphere, it is predicted that the line-of-sight propagation with improved directivity using beamforming will become mainstream [4].

Antennas that emit and receive directional terahertz waves inside mobile devices are one of the extremely important elements for the realization of beyond 5G/6G. In addition to mobile antennas, compact and high-gain immobile antennas are also required for converters between wireless and fiber communications, which is the core of terahertz radio-over-fiber technology [5], [6]. The common base that supports these antennas is a coupling structure that transfers waves in free space into waveguides. One of the well-known coupling structures is a combination of a horn antenna and a hollow metal waveguide. Some reports have been made even in the terahertz band [7], [8], [9]. However, horn antennas require a sufficient length to be coupled to a waveguide, making them unsuitable for mobile devices due to their size. Another structure is a combination of a metal planar antenna and a metal planar waveguide, which is used in the conventional mobile devices [10], [11], [12], [13]. Although commonly used, the Ohmic loss of metal in the terahertz band is larger than that in the low-frequency band. Therefore, even microstrip lines and coplanar lines conventionally used in the millimeter wave band are considered difficult to apply in the terahertz band [14]. Moreover, dielectric waveguides that confine the electromagnetic field within a dielectric material with lower absorption, such as dielectric image lines, nonradiative dielectric waveguides, and silicon waveguides, are desirable [15], [16], [17], [18], [19], [20]. The antenna could also be constructed from a low-loss dielectric material instead of metal [21]. However, dielectric structures, such as lenses, require sufficient optical path length to focus electromagnetic waves and couple them into a waveguide, making them inappropriately large for mobile devices, as are horn antennas.

Surface plasmon polariton is a phenomenon in which an electromagnetic wave interacts with electrons on the metal surface

and propagates along the metal surface. Many applications based on this phenomenon are already known [22], [23], [24], [25], [26]. Among them, the bull's eye structure is a typical structure that focuses electromagnetic waves based on surface plasmon polaritons and has been proposed for a wide range of frequencies from visible to terahertz bands [27], [28], [29], [30], [31], [32], [33], [34]. In the terahertz band, it is generally believed that surface plasmon polaritons do not exist on flat metal surfaces, but subwavelength periodic structures allow their coupling on metal surfaces, known as spoof surface plasmon polaritons [35], [36], [37]. A bull's eye structure has a concentric periodic structure resembling a bull's eye. Thus, spoof surface plasmon polaritons are excited at the resonant frequency corresponding to the structural period and propagate toward the center of concentric structure. When an aperture is formed in the center, an enhanced transmission called extraordinary optical transmission occurs, which cannot be seen with a subwavelength aperture alone [38]. In fact, it has been pioneered that this wave-focusing phenomenon can be explained by the theory that waves propagating on metal periodic structures, described above as spoof surface plasmon polaritons, are leaky waves [39], [40], [41]. Since the above phenomenon occurs on the surface rather than in space, it is possible to create antennas that are much thinner than dielectric lenses and horn antennas. Therefore, by coupling the wave confined to the subwavelength aperture into a waveguide, it is expected to create a thin and compact antenna that can be applied to the next-generation mobile communications.

In addition to the above practical demands, there has been increasing interest in freely controlling the coupling nature itself. In the optical region, it has been reported that the propagation direction of coupled waves into a waveguide can be controlled by the polarization state of waves incident on a nanoparticle as a scatterer placed near the waveguide [42], [43]. This symmetry breaking phenomenon is understood as the spin-orbit interaction of light, by analogy with that of electrons, and is expected to be applied to optical communications. Similarly, in the terahertz region, it is predicted that not only the direction control but also the phase control will be possible by exciting waveguide propagation modes using the near field of a subwavelength aperture with a bull's eye structure [44]. In order to seamlessly connect terahertz and optical communications, flexible coupling control of terahertz waves is also necessary.

In this study, we propose a method to couple terahertz waves confined in a subwavelength aperture by a bull's eye structure into a planar dielectric waveguide placed on the opposite side of the substrate while controlling the phase. Fig. 1 shows a conceptual diagram of the proposed device. The copper-plated substrate has concentric grooves with subwavelength periods and a subwavelength aperture in the center, that is, a bull's eye aperture. A waveguide made of silicon is placed on the opposite side of the substrate. If the side with the bull's eye structure is defined as the backside of the substrate, the silicon waveguide is on the frontside. The silicon waveguide formed on copper functions as a dielectric image line that transmits terahertz waves. When the longitudinal direction of the waveguide is the x-axis, spoof surface plasmon polaritons excited by the backside bull's eye structure with x-polarized incidence are transmitted

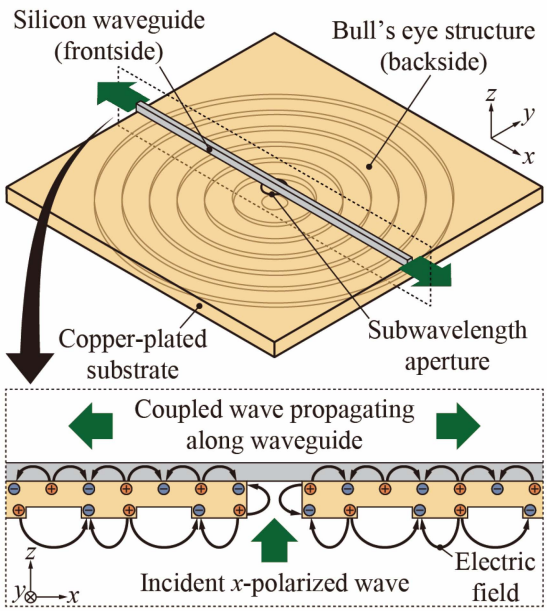

Fig. 1. Conceptual diagram of spoof surface plasmon coupling from the backside bull's eye aperture into the frontside silicon waveguide.

to the frontside through the aperture and excite a coupled wave propagating along the silicon waveguide. In addition, we also reveal the coupling manner in a Y-branched waveguide instead of a straight waveguide and demonstrate the phase control depending on the incident polarization. Phase control enables unidirectional propagation on a waveguide. Therefore, it offers the possibility of controlling of the three degrees of freedom of the amplitude, phase, and direction of waves propagating on a waveguide by the amplitude, phase, and polarization of the incident wave in free space.

II. Design and Simulation

We first defined the parameters regarding the dimensions of the proposed device. Fig. 2 shows a schematic diagram of each part of the proposed device. Fig. 2(a) shows the backside and frontside of the copper-plated substrate alone. When viewed from the backside, grooves with an aperture in the center are formed. There are no grooves on the frontside, only the aperture. An aperture with a diameter d is formed in a substrate with a thickness s, and a groove with a width w and a height h is formed with a period p around the aperture.

A silicon waveguide is placed on the frontside of the substrate to guide the coupled wave excited through the aperture. Fig. 2(b) shows a straight silicon waveguide placed over the aperture from the frontside. The waveguide passes through the center of the aperture and has dimensions of height a and width b. The dimensions of the silicon waveguide must be selected appropriately according to the desired propagation mode [15]. One end of the straight waveguide is defined as Port 1, and the other end is defined as Port 2.

Fig. 2(c) shows a Y-branched silicon waveguide placed instead of a straight waveguide. An arc part with a radius r and a central angle γ extends from the branch point, and the end thereof is

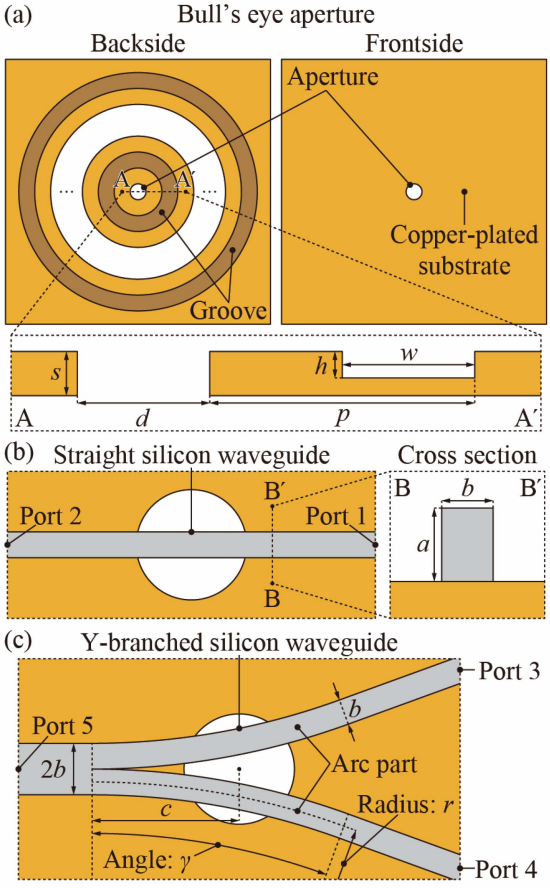

Fig. 2. Schematic diagrams of (a) bull's eye aperture, (b) straight silicon waveguide, and (c) *Y*-branched silicon waveguide.

connected to a straight waveguide. The width of the waveguide before branching is $2b$, and after branching, each waveguide has a width b. The height of the waveguide is a. The center line of the *Y*-shape passes through the center of the aperture, and the branch point is located at a distance c from the center of the aperture. The two branched ends are defined as Ports 3 and 4, and the end before branching is defined as Port 5. It is worth mentioning that the *Y*-branched waveguide itself has already been reported for splitters and combiners in the terahertz region, as well as for near-field probing applications [45], [46].

Next, we investigated the propagation of spoof surface plasmon polaritons on the bull's eye structure and coupled waves on the waveguide using electromagnetic field simulation software based on finite-element analysis (COMSOL Multiphysics, COMSOL, Inc.). Frequency-domain solver in the wave optics module of COMSOL Multiphysics was used to solve a time-harmonic electromagnetic problem [47]. The mesh size was set to be one-sixth or less of the incident wavelength. The relative tolerance was set to 0.001. Fig. 3(a) shows a schematic diagram of the simulation model. The waveguide part was made of silicon with a refractive index of 3.4. The remaining parts were made of air with a refractive index of 1. The surface of the bull's eye aperture was defined as a perfect electric conductor (PEC). For the proposed device, the calculated results were almost the same as in the case of PEC even when the finite conductivity

TABLE I
PARAMETER VALUES IN SIMULATION

d [μm]	s [μm]	w [μm]	h [μm]	p [μm]	a [μm]	b [μm]	c [μm]	r [μm]	γ [°]
300	100	300	60	600	100	70	400	2000	20

was taken into account (see Fig. S1 in Supplementary Material). Note that Fig. 3(a) shows a cross section of the model; in other words, the entire model was 3-D, and the part of the bull's eye aperture, except for the waveguide, was axisymmetric around the z-axis. A Gaussian beam was incident from the wave source coaxially with the center of the bull's eye aperture. In addition, in order to calculate the transmittance of the bull's eye aperture and that after coupling and propagating to the waveguide, power monitors were set at a position above the frontside surface and at the ends of the waveguide.

For the following simulation, we set the parameter values, as summarized in Table I. Aiming for a device that functions around the 0.5 THz band, the period of the bull's eye structure p was made to match the wavelength of 600 μm in free space [28]. The total diameter of the bull's eye aperture substrate was 9000 μm, and six grooves were made on it. It is worth mentioning that even if the number of grooves is increased, the transmission enhancement gradually saturates [27]. The end faces of the silicon waveguide were located at the circumference of the substrate. The radius of the beam waist and the electric field amplitude at the beam center of the Gaussian beam were 3000 μm and 1 V/m, respectively. The distance from the backside surface of the bull's eye aperture to the wave source and that from the frontside surface to the power monitor above it were both 750 μm.

Fig. 3(b) shows the calculated transmittances normalized by the maximum value at the transmission peak. The transmittance of the bull's eye aperture was calculated from a power monitor above the frontside surface using a model without waveguides. The transmittance of the coupled wave to the waveguide was calculated from a power monitor placed at the end face of straight waveguide. The bull's eye aperture alone showed a unimodal transmission peak at 0.492 THz. This value is slightly lower than 0.5 THz, which is the frequency of a wave with the same wavelength as the period of the grooves, 600 μm. The peak was asymmetrical and steeper on the high-frequency side than on the low-frequency side. These characteristics are consistent with the previous literature [29]. In addition, the full width at half maximum (FWHM) was 33 GHz, and the quality factor (QF) calculated by dividing the FWHM by the resonant frequency, 0.492 THz, which indicates the sharpness of the peak, was 15. The spectrum of the coupled wave into the silicon waveguide showed a similar shape.

Fig. 3(c)–(h) shows the calculation results of the z-axis component of the electric field at 0.492 THz. Fig. 3(c) shows the frontside surface of a model without waveguides viewed from the $+z$-axis direction. Fig. 3(d) shows its cross section passing through the center of the aperture viewed from the $-y$-axis direction. The incident polarization was in the x-axis direction. As can be seen from Fig. 3(d), an electric field is generated

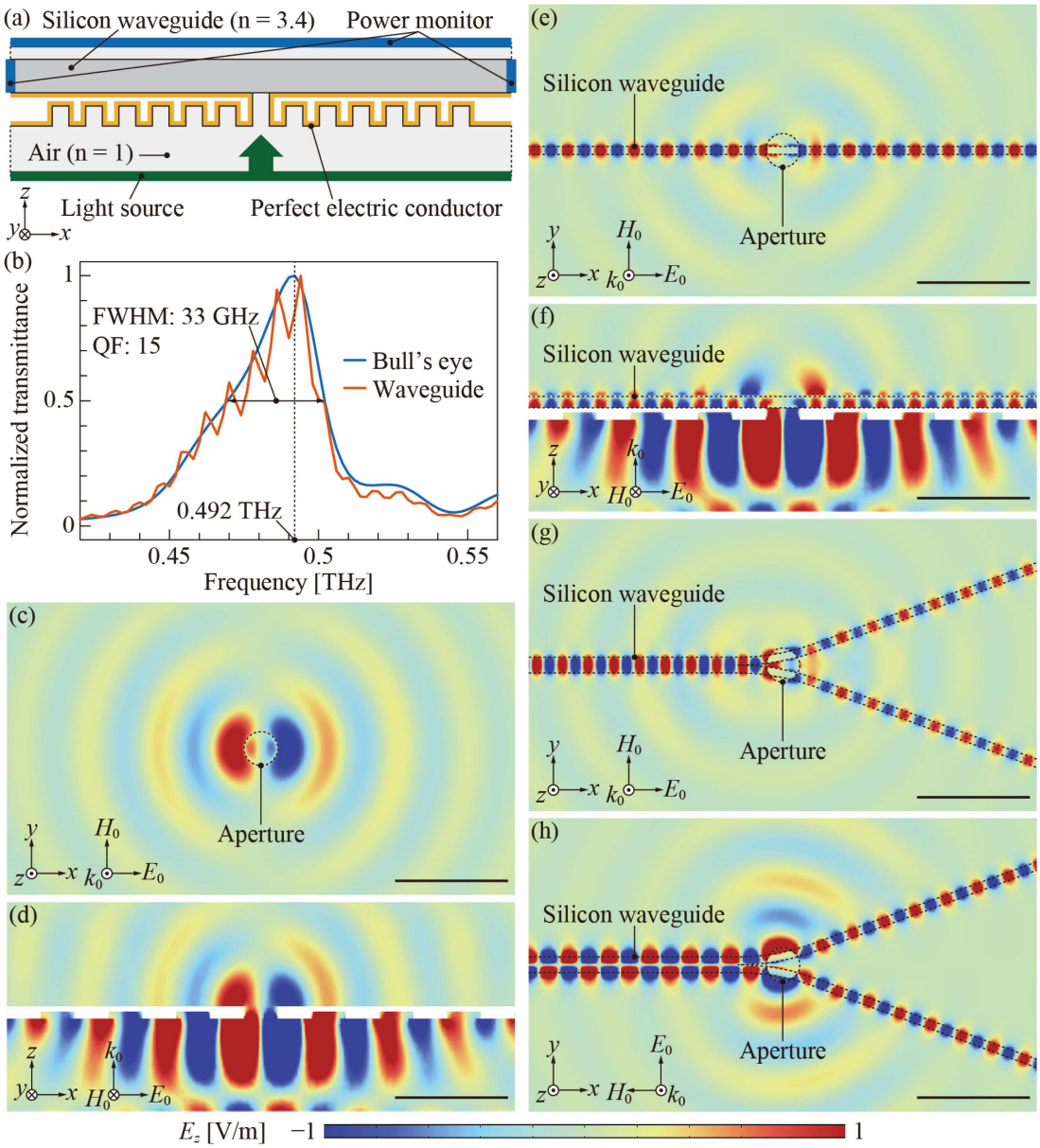

Fig. 3. (a) Schematic diagram of the simulation model. (b) Calculated normalized transmittances after passing through a bull's eye aperture alone and that after coupling and propagating into a straight silicon waveguide. (c–h) z-axis component of the calculated electromagnetic fields. E_0, H_0, and k_0 represent the electric field, magnetic field, and wave vector of the incident wave, respectively. (c) Front and (d) cross-sectional views on a bull's eye aperture without waveguides. (e) Front and (f) cross-sectional views on a bull's eye aperture with a straight waveguide. Front views on a bull's eye aperture with a Y-branched waveguide with (g) x-polarized incidence and (h) y-polarized incidence. The colors used to represent the electric field are displayed on the gradation of the color bar if it is between -1 and 1 V/m. If it is less than -1 V/m or more than 1 V/m, the color is the same as the minimum or maximum value, respectively. Scale bars: 1000 μm.

periodically along the grooves, and its strength increases toward the aperture. The electric field leaks from the backside to the frontside through the aperture. Then, the wave propagates along the frontside conductor surface. As shown in Fig. 3(c), the wave propagates from the center while spreading in the x-axis direction, which corresponds to the incident polarization, and has opposite phases in the $+x$ and $-x$ directions.

Fig. 3(e) shows the frontside surface of a model with a straight waveguide viewed from the $+z$-axis direction. Fig. 3(f) shows its cross section passing through the center of the aperture viewed from the $-y$-axis direction. The incident polarization was in the x-axis direction. As shown in Fig. 3(e), compared to the case without waveguides, the coupled wave propagates along the waveguide. Furthermore, as shown in Fig. 3(f), although there is some leakage at the silicon–air interface, most of the propagating waves propagate through the conductor–silicon interface. The wavelength of the coupled wave is approximately 265 μm, which is approximately 2.3 times smaller than the wavelength in air, 609 μm. Therefore, the effective refractive index of this waveguide coupling mode is considered to be 2.3. Note that no coupling to the waveguide was observed when the incident polarization was in the y-axis direction.

Fig. 3(g) shows the frontside surface of a model with a Y-branched waveguide viewed from the $+z$-axis direction when

the incident polarization was in the x-axis direction. Fig. 3(h) shows the result when the incident polarization was in the y-axis direction. Unlike a straight waveguide, coupling also occurs for a y-polarized wave. Considering the phase difference between the branched waveguide ports (Port 3 and Port 4), the x-polarized wave gives the same phase, and the y-polarized wave gives the opposite phase. It is known that when the coupling to the waveguide has a dependence on the incident polarization, the phase difference at each port can be controlled [44]. If the electric field of the coupled wave to each port with x- and y-polarization incidence is expressed as $E_{\mathrm{Port3},x}$, $E_{\mathrm{Port3},y}$, $E_{\mathrm{Port4},x}$, and $E_{\mathrm{Port4},y}$, the combined electric field at each port, E_{Port3} and E_{Port4}, with polarization incidence rotated by θ from the x-axis is expressed as follows:

$$E_{\mathrm{Port3}} = E_{\mathrm{Port3},x} \cos\theta + E_{\mathrm{Port3},y} \sin\theta \tag{1}$$

$$E_{\mathrm{Port4}} = E_{\mathrm{Port4},x} \cos\theta + E_{\mathrm{Port4},y} \sin\theta. \tag{2}$$

Furthermore, considering that the phase at each port is reversed with respect to the incident polarization direction, $E_{\mathrm{Port3},x}$, $E_{\mathrm{Port3},y}$, $E_{\mathrm{Port4},x}$, and $E_{\mathrm{Port4},y}$ are expressed as follows:

$$\begin{pmatrix} E_{\mathrm{Port3},x} \\ E_{\mathrm{Port4},x} \end{pmatrix} = A\mathrm{e}^{i\alpha} \begin{pmatrix} 1 \\ 1 \end{pmatrix} e^{-i\omega t} \tag{3}$$

$$\begin{pmatrix} E_{\mathrm{Port3},y} \\ E_{\mathrm{Port4},y} \end{pmatrix} = B\mathrm{e}^{i\beta} \begin{pmatrix} 1 \\ -1 \end{pmatrix} e^{-i\omega t}. \tag{4}$$

Here, A and B are the amplitude transmittances, α and β are the phase delays, ω is the angular frequency of wave, and t is the time. In the ideal case, where $A = B$ and $\beta - \alpha = 90°$, the following equation holds from (1) to (4)

$$\begin{pmatrix} E_{\mathrm{Port3}} \\ E_{\mathrm{Port4}} \end{pmatrix} = A \begin{pmatrix} e^{i\theta} \\ e^{-i\theta} \end{pmatrix} e^{-i(\omega t - \alpha)}. \tag{5}$$

Obviously, the phase difference between Port 3 and Port 4 is 2θ; thus, by rotating the polarization by 90°, it is possible to change the phase difference from 0° to 180°. From the simulation results, the parameters A, B, and $\beta - \alpha$ related to the coupling in the Y-branched waveguide were determined to be 0.65°, 0.8°, and 129°, respectively. Although this device does not perfectly match the ideal case, phase control based on the polarization dependence of coupling is expected. In this study, we actually fabricate the device and experimentally verify its phase controllability.

III. Fabrication

We fabricated the proposed device based on silicon micromachining. Fig. 4 shows the fabrication processes. The bull's eye aperture and silicon waveguides were fabricated separately and later bonded together. For the bull's eye aperture, we first prepared a cleaned silicon substrate of 20 mm × 20 mm × 0.1 mm as a starting substrate. Second, a photoresist pattern for the grooves was formed using photolithography. Third, silicon was etched to a depth of 60 μm using deep reactive ion etching (DRIE). Fourth, the photoresist was patterned for the aperture by photolithography on the side opposite the grooves. Fifth, the aperture was formed through etching with DRIE. Sixth, the

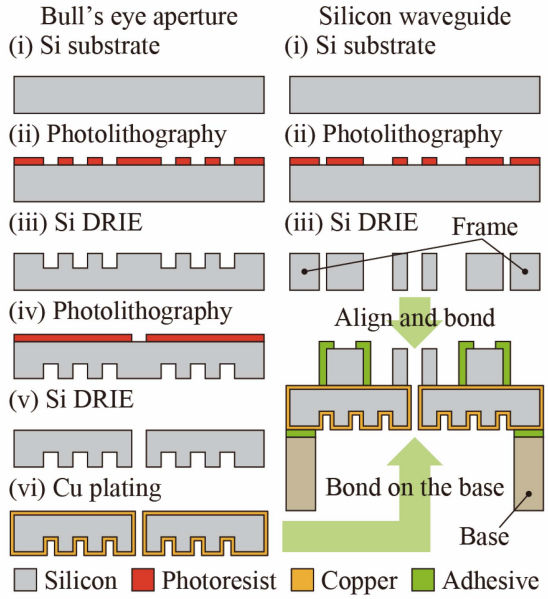

Fig. 4. Schematic diagram of the fabrication processes.

silicon surface was coated with copper by electroless copper plating (Circuposit 6530, DDP Specialty Products Japan K.K.) using a primer (ML-1440, IOX Co., Ltd.). Fig. 5(a) shows the fabricated bull's eye aperture with ten grooves. It was confirmed that the entire part, including the grooves and aperture, was copper plated.

For the silicon waveguide, we first prepared a cleaned silicon substrate of 20 mm × 20 mm × 0.1 mm as a starting substrate. Second, a photoresist pattern was formed using photolithography. Third, silicon was etched through with DRIE. Because it is difficult to hold a thin and fragile waveguide alone, two support parts connected to the waveguide with four beams are built, which are also connected to the frame by beams. The frame was handled during assembly and was removed after bonding the support parts to the bull's eye aperture. Fig. 5(b) shows the fabricated Y-branched silicon waveguide. The width of the beam connecting the support part and the waveguide was 70 μm, and the length was 1200 μm. Elliptical joints are used to suppress propagation loss [48]. The ends of the waveguide are tapered over a length of 1500 μm, allowing waves propagating through the waveguide to exit into free space.

To assemble them, we first attached the bull's eye aperture onto a base made of acrylonitrile-butadiene-styrene resin using a 3-D printer. The epoxy adhesive was used for bonding. Note that the base was not required for the device itself but was attached because it facilitates handling during experiments. Next, the waveguide was aligned to the aperture under microscope observation and bonded to the bull's eye aperture. During bonding, deionized water was dropped onto the substrate, and after alignment, it was allowed to air dry for temporary bonding. After that, the area around the support parts other than the waveguide was bonded using epoxy adhesive. Afterward, the frame was removed by destroying the beams connecting to the support parts. Fig. 5(c) and (d) shows a device with a Y-branched

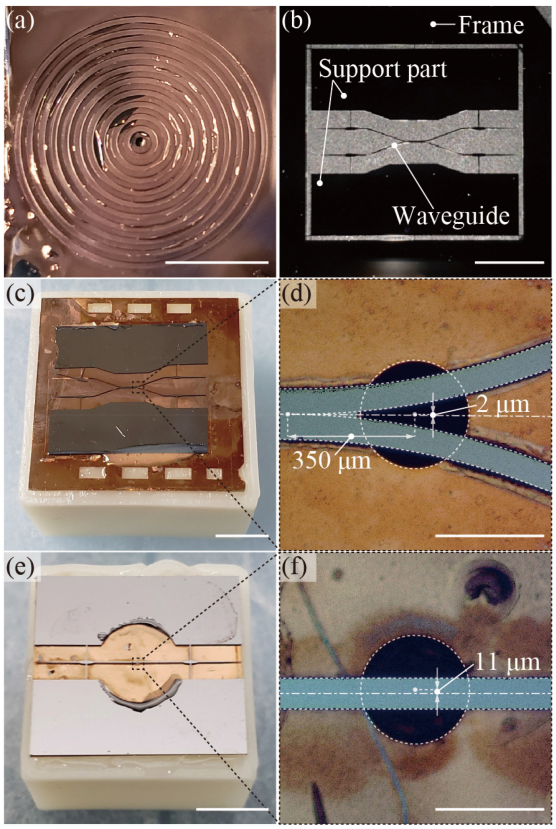

Fig. 5. Photographs of (a) bull's eye antenna, (b) *Y*-branched waveguide, (c) fabricated device with a *Y*-branched waveguide, (d) enlarged view of the vicinity of the aperture with the *Y*-branched waveguide, (e) fabricated device with a straight waveguide, and (f) enlarged view of the vicinity of the aperture with the straight waveguide. Scale bars: (a–c and e) 1000 μm. (d and f) 300 μm.

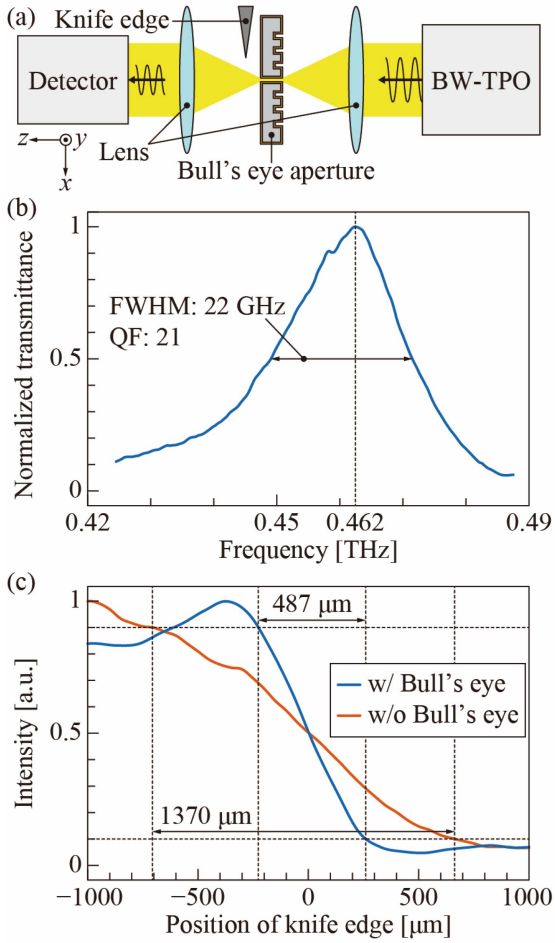

Fig. 6. (a) Schematic diagram of the experimental setup for the evaluation of the bull's eye aperture. (b) Measured transmittance of the fabricated bull's eye aperture. (c) Measurement results of beam focusing using the knife-edge method with and without the bull's eye aperture.

waveguide and its enlarged view of the vicinity of the aperture, respectively. The alignment error between the center line of *Y*-branched waveguide and the center of aperture was 2 μm. The distance between the branched point and the center of aperture was 350 μm. Note that the length measurement was based on the fitting line because the branched point in the actual device was rounded to avoid stress concentrations. Fig. 5(e) and (f) shows a device with bonded straight waveguides and its enlarged view of the vicinity of the aperture, respectively. The alignment error between the center line of straight waveguide and the center of aperture was 11 μm.

IV. Experiment and Result

A. Evaluation of the Bull's Eye Aperture

We first evaluated the transmission characteristics of the fabricated bull's eye aperture alone. Fig. 6(a) shows the experimental setup. A backward terahertz-wave parametric oscillator (BW-TPO) was used as the monochromatic and frequency-tunable terahertz-wave source [49], [50], [51]. A lens with a focal length of 50 mm (Tsurupica, Pax Co.) focused the wave onto the bull's eye aperture, and the transmitted wave was again collimated with a lens with a focal length of 50 mm and entered the detector (3DL 12C LS2500 A1, ACST GmbH). Using the state without the bull's eye aperture as a reference, the transmitted intensity was measured in the frequency range from 0.42 to 0.49 THz. When evaluating the focusing ability of the beam, a knife edge was inserted behind the bull's eye aperture, and the transmitted intensity was measured.

Fig. 6(b) shows the measured transmittance of the bull's eye aperture. To focus only on the shape of spectrum, the transmittance was normalized by the peak value. The FWHM and QF were 22 GHz and 21, respectively. Compared with the simulation, the shape of the spectrum was consistent in which there was a unimodal peak, which was slightly steeper on the high-frequency side than on the low-frequency side. The resonant frequency of the fabricated sample was 0.462 THz, which was lower than the simulation result of 0.492 THz.

Fig. 6(c) shows the evaluation results of beam focusing using the knife-edge method. The incident frequency was 0.462 THz. When the position of the knife edge was moved from −1000 to 1000 μm, the beam was blocked, and the intensity decreased. It is known that the beam diameter can be determined from the distances at which the transmitted intensity is 10% and 90% [52]. The intensities, as shown in Fig. 6(c), are normalized so that the maximum value is 1. The distance between the 10% and 90%

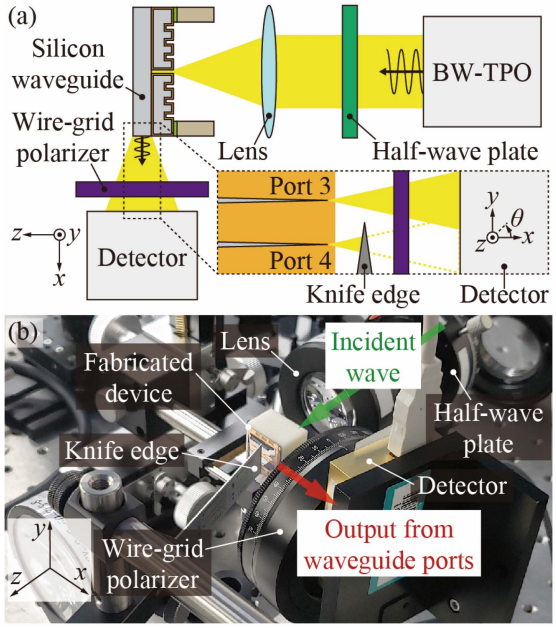

Fig. 7. (a) Schematic diagram and (b) photograph of the experimental setup for the evaluation of the antenna–waveguide coupling device.

positions was 487 μm with a bull's eye aperture and 1370 μm without it, that is, the wave was focused by a lens. Compared with the wavelength of 649 μm at a frequency of 0.462 THz, when the bull's eye aperture was used, the wave was focused on the subwavelength size.

B. Evaluation of the Aperture–Waveguide Coupling Device

Next, we evaluated the transmission characteristics of a device in which a waveguide was bonded to a bull's eye aperture. Fig. 7(a) and (b) shows a schematic diagram and a photograph of the experimental setup, respectively. The terahertz waves emitted from the BW-TPO passed through a half-wave plate to control the polarization angle and entered the bull's eye aperture through a lens with a focal length of 50 mm. The detector was placed near the end of the waveguide via a wire grid polarizer (WGP). In the case of the *Y*-branched waveguide, the interfered wave from both ports was first measured. Then, one side of the ports was blocked with a knife edge, and the output from each port was measured.

Fig. 8(a) shows the output intensity measured when a *x*-polarized or *y*-polarized wave was incident in the frequency range of 0.42–0.49 THz. It shows the individual outputs from Ports 3 and 4 and the interfered output from both ports. The transmission axis of WGP was in the *z*-axis direction. When inputting a *x*-polarized wave, the interfered output from both ports exceeded the individual outputs from Ports 3 and 4 across all frequency ranges. Also, even the sum of the outputs of Ports 3 and 4 was smaller than the interfered output value. This is thought to be because the outputs from both ports are waves that are in phase, causing constructive interference. When a *y*-polarized wave was input, the interfered output from both ports was roughly the same as the output from Port 4 in the

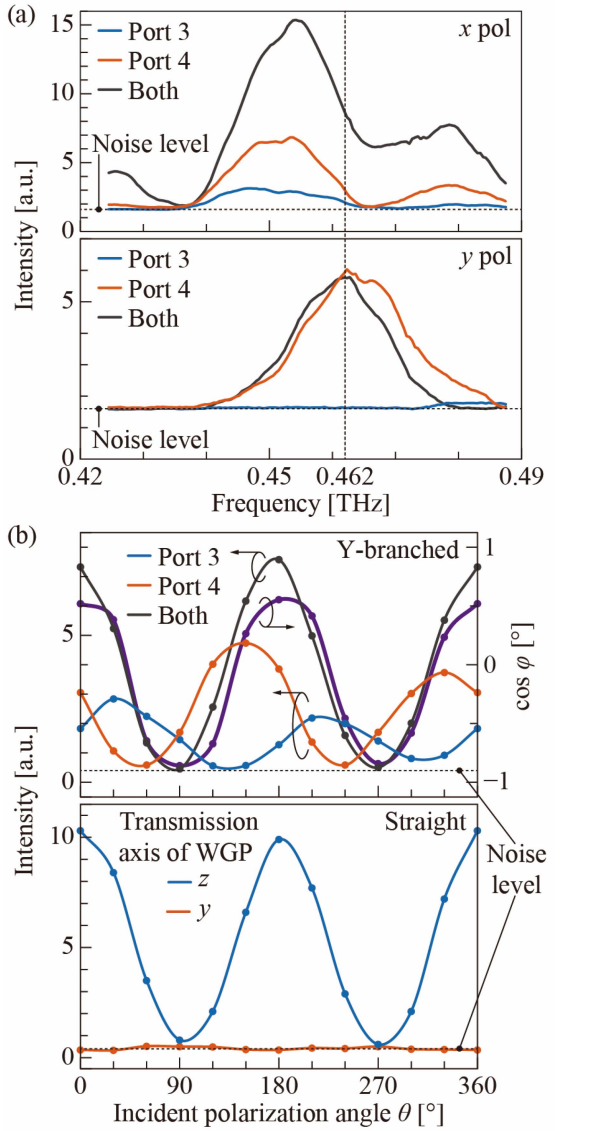

Fig. 8. (a) Output intensity spectra from the fabricated device with a *Y*-branched waveguide when irradiated with an *x*-polarized or *y*-polarized wave. (b) Output intensity at 0.482 THz when irradiating a *Y*-branched or straight waveguide while changing the incident polarization angle.

range of 0.42–0.46 THz, and Port 4 was larger at 0.46 THz or higher. In addition, at 0.48 THz or higher, the output from Port 3 also exceeded the interfered output. This is thought to be that the outputs from both ports are waves with opposite phases, causing destructive interference.

Comparing with Fig. 6(b), when a *y*-polarized wave was incident, a single peak appeared around 0.462 THz, which was the same as the bull's eye aperture alone, whereas multiple peaks were seen with an *x*-polarized wave. The reason for these multiple peaks is probably because when an *x*-polarized wave was incident, a part of the spoof surface plasmon polariton coupled onto the bull's eye structure may be radiated into space from the substrate edge, causing interference with radiation from the waveguide end. When a *y*-polarized wave was incident, it seems that it was coupled to the waveguide while maintaining the same

transmission spectrum shape as the bull's eye aperture alone, similar to the simulation result, as shown in Fig. 3(b). Also, when a *y*-polarized wave was input, an output intensity above the noise level could not be obtained at Port 3 below 0.48 THz. We speculate that the reason for this is that the radiation pattern at the end of the waveguide was disrupted due to manufacturing errors, such as bonding, and the waves did not reach the detector properly.

At 0.482 THz, where the output at Port 3 was confirmed when a *y*-polarized wave was incident, measurements were performed while the half-wave plate was rotated 180° in 15° increments; thus, the incident polarization angle was rotated 360° in 30° increments. Fig. 8(b) shows the measurement results for the device with a *Y*-branched or straight waveguide. In the case of the *Y*-branched waveguide, the interfered wave from both ports and output from each port are shown together. The incident polarization angle θ was defined as the angle from the $+x$-axis toward the $+y$-axis when viewed from the $+z$-axis direction, as shown in Fig. 7(a). First, when rotating the incident polarization angle from 0° to 30°, the output of Port 3 increased and the output of Port 4 decreased. Then, the output of Port 3 reached its maximum value around 30°, and the output of Port 4 took its minimum value around 60°, below the noise level. This is because the waveguide branched near the aperture is tilted by 20°, which is the central angle of the arc part. The polarization direction was parallel to the waveguide when the incident polarization angle was 20° for Port 3, achieving the maximum coupling efficiency. On the other hand, it was perpendicular to the waveguide when the incident polarization angle was 70° for Port 4, achieving the minimum coupling efficiency. After that, extrema appeared every 90° in both Port 3 and Port 4, suggesting that it was a trigonometric function related to 2θ. Regarding the interfered wave from both ports, the maximum value was taken at 0° (360°) and 180°, that is, *x*-polarization, and the minimum value was taken at 90° and 270°, that is, *y*-polarization. This agrees with the observation obtained from Fig. 8(a) that the outputs from both ports have the same phase when *x*-polarized and *y*-polarized have opposite phases.

Next, we considered the phase difference φ between Port 3 and Port 4 based on the measurement results. If the intensities of the waves output from Port 3 and Port 4 are I_3 and I_4, respectively, and that of the interfered wave from both ports is I, the following equation holds true

$$\cos\varphi = \frac{(I_3 + I_4) - I}{2\sqrt{I_3 I_4}}. \tag{6}$$

Note that (6) is derived from the law of cosines regarding the resultant electric field (see Fig. S2 in Supplementary Material). Although the value of φ cannot be determined by intensity measurement alone, if the phase controllability shown in (5) holds true, the value of φ is expected to be 2θ. Fig. 8(b) also shows the value of $\cos(\varphi)$ calculated using (6) from the measurement results for each incident polarization angle. The result was close to $\cos(2\theta)$. One possible reason why the minimum value does not reach -1 is that when θ is 90° or 270°, the interfered output of both ports does not become 0 and is limited by the noise level. Also, the reason why the maximum value does not reach 1 is that when θ is 0° or 180°, that is, *x*-polarization, interference due to radiation of the spoof surface plasmon polariton is included as background noise.

Finally, in the case of the straight waveguide, the transmission axis direction of the WGP was set as the *z*-axis or *y*-axis, as shown in Fig. 8(b). When the transmission axis was in the *y*-axis direction, the output was below the noise level. On the other hand, when it was in the *z*-axis direction, it was confirmed that the output depended on the incident polarization angle. This result shows that the output from the waveguide is *z*-polarized, suggesting that the waves were coupled into the waveguide, as considered in Fig. 3(e) and (f), and emitted into free space. In addition, when θ was 90° or 270°, the straight waveguide produced an output equivalent to the noise level, whereas the *Y*-branched waveguide produced an output above the noise level from each port alone, which is also evidence that waves were coupling and propagating from the aperture to the waveguide.

C. Discussion

Based on the above results, we demonstrated for the first time that aperture–waveguide coupling was possible via spoof surface plasmon polaritons by placing a silicon waveguide over the bull's eye aperture. The greatest advantage of this device over conventional coupling structures is its thinness, which is extremely advantageous for mounting on mobile devices. The combined thickness of the bull's eye aperture and waveguide is 200 μm, whereas a horn antenna in the same frequency band requires a length of several tens of millimeters [7]. The origin of this feature is based on two effects. One is that the spoof surface plasmon polaritons are generated by the bull's eye aperture and focused on the aperture. The other is that the spoof surface plasmon polaritons couple into the waveguide on the opposite surface. We also revealed that phase control with the incident polarization angle was possible by using a *Y*-branched waveguide. Linearly polarization incidence was used in this study. However, it is known that extending to circularly polarization allows unidirectional propagation because the amplitude and phase of each port can be controlled independently [44]. In recent years, in addition to frequency multiplexing and spatial multiplexing, polarization multiplexing has attracted attention in order to efficiently utilize limited bandwidth [53]. The proposed device can separate orthogonal polarizations into different waveguide ports, which enables polarization multiplexing with a single antenna.

In order to further examine the basic characteristics of the proposed device as a receiving antenna, additional simulations were performed with different incident angles and polarizations. Fig. 9 shows the receiving pattern and the phase difference between Ports 3 and 4, φ, when the incident angle η is changed. As shown in the inset in Fig. 9(a), η was changed around the *y*-axis, which is orthogonal to the axis of symmetry of the *Y*-branched waveguide. A plane wave was used for the calculation, whose wavenumber vector was expressed as $k = ((2\pi/\lambda)\sin(\eta), 0, (2\pi/\lambda)\cos(\eta))$, where λ was the wavelength in free space. To calculate the gain G, the effective area A_{eff} was first calculated, which was the ratio of the power at the waveguide end to

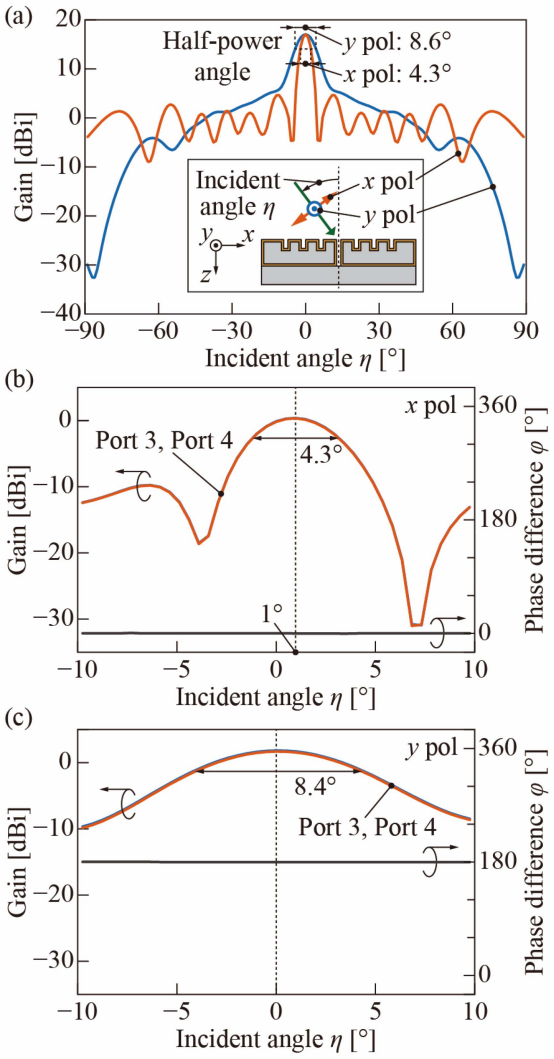

Fig. 9. Simulation results of receiving patterns for (a) bull's eye aperture alone, (b) bull's eye aperture with a *Y*-branched waveguide with *x*-polarized incident, and (c) *y*-polarized incident. Phase difference between Port 3 and Port 4 was also calculated in (b) and (c).

the power density in free space. Then, it was converted to G using the relational expression $A_{\text{eff}} = (\lambda^2/4\pi)G$ [54]. The same procedure was performed when changing the incident angle around the *x*-axis (see Fig. S3 in Supplementary Material). Fig. 9(a) shows the receiving pattern of a bull's eye aperture alone. The maximum gain was on the broadside, with a value of 17.0 dBi. The dependence on the incident angle was different for *x*- and *y*-polarization. The half-power beamwidth (HPBW) was 4.3° for *x*-polarization and 8.6° for *y*-polarization. This result corresponds to the fact that the HPBW becomes narrower in the polarization direction even when radiating from the bull's eye aperture [27]. Fig. 9(b) and (c) shows the results when *x*-polarized and *y*-polarized waves are incident on a bull's eye aperture with a *Y*-branched waveguide, respectively. The receiving patterns of Ports 3 and 4 overlapped due to the symmetry of the *Y*-branched waveguide. For *x*-polarization, the maximum gain was located +1° away from the broadside, with a value of 0.3 dBi, which means that the gain is higher when the incident wave enters from the opposite direction of ports across the aperture. A similar trend was observed for *y*-polarization, although the maximum gain of 1.7 dBi was observed closer to the broadside. The HPBW was 4.3° for *x*-polarization and 8.4° for *y*-polarization. The phase difference φ was approximately 0° for *x*-polarization and 180° for *y*-polarization, regardless of the incident angle in the HPBW range, which allows phase control based on the incident polarization direction.

In the prototype we designed this time, waveguides were placed directly over the aperture. Although we were able to demonstrate the phase controllability of our device, the coupling efficiency from the aperture to the waveguide was not sufficient. As shown in Fig. 9, in the case of *x*-polarization, the gain decreases from 17.0 to 0.3 dBi at the end of waveguide compared with the case of a bull's eye aperture alone, which means that only about 2% of the power was coupled into the waveguide. On the other hand, when a hollow metal waveguide is connected vertically to the aperture of bull's eye aperture, a coupling efficiency of 90% can be obtained [27]. In our device, much of the power transmitted through the aperture is radiated again. Structures around the aperture that efficiently couple the focused waves into waveguides need to be further explored. Another solution is to increase the gain of the bull's eye aperture alone, which would require optimization of the structure, such as adding a Bragg reflector, changing the aperture shape, and using Fabry–Pérot resonances [29], [30], [55]. A recent study reported that complementary split-ring apertures can reduce the sidelobe level and improve the directivity of bull's eye structure [56]. Practically, it is also important to reduce the propagation loss after coupling by making the copper plating uniform and smoothing the sidewalls of the silicon waveguide [57]. It has been pointed out that surface roughness associated with fabrication leads to losses, such as scattering and phase mismatch in the propagation of spoof surface plasmon polaritons, which cannot be estimated simply by applying an effective conductivity [58]. Our proposed method still has major challenges in terms of efficiency. Therefore, improvements are needed that take the above points into account.

The bull's eye aperture itself has broadside directivity and is not an antenna capable of beamforming. However, in recent years, reconfigurable metasurfaces driven by various methods, such as liquid crystal, graphene, phase transition materials, and microelectromechanical systems, have been developed that can control the phase distribution of beam and bend the optical path [59], [60], [61], [62], [63], [64]. By combining them with our device, dynamic control of antenna characteristics will be expected. Furthermore, since the wave-focusing mechanism of our device is based on spoof surface plasmon polaritons on the bull's eye structure, other structures based on them are also available, making the coupling between the aperture and waveguide more functional. For example, a Bessel beamformer would be beneficial for near-field probing [65].

The fabrication of the proposed device is based on silicon micromachining, which is suitable for the collective fabrication of a large number of elements required for future mobile devices. It is also compatible with silicon-based elements for steering terahertz waves [18], [19], [20], [21], [66]. Structures that can

be formed using silicon micromachining have dimensions comparable to the wavelengths of terahertz waves, 30–3000 μm, and are believed to be necessary to develop a wide variety of devices to realize beyond 5G/6G.

V. Conclusion

We proposed a method of coupling from a bull's eye aperture to a planar silicon waveguide via spoof surface plasmon polaritons in the terahertz band. A device combining a bull's eye aperture that functions in the 0.5 THz band with a straight or *Y*-branched silicon waveguide was designed using electromagnetic field simulation and fabricated using silicon micromachining and copper plating. The transmission peak of the bull's eye aperture alone was observed at 0.462 THz. In a device with a straight waveguide, directional propagation was confirmed in which only linearly polarized waves parallel to the waveguide were coupled. In a device with a *Y*-branched waveguide, the phase controllability between the two waveguide ports according to the incident polarization angle was confirmed. This device realizes the thin and compact phase controllable coupling required for the next-generation mobile communication, beyond 5G/6G.

Acknowledgment

A part of this work was performed at Micro/Nano-Machining Research and Education Center, Tohoku University.

References

[1] J. Federici and L. Moeller, "Review of terahertz and subterahertz wireless communications," *J. Appl. Phys.*, vol. 107, 2010, Art. no. 111101, doi: 10.1063/1.3386413.

[2] T. S. Rappaport et al., "Wireless communications and applications above 100 GHz: Opportunities and challenges for 6G and beyond," *IEEE Access*, vol. 7, pp. 78729–78757, 2019, doi: 10.1109/ACCESS.2019.2921522.

[3] U. Gustavsson et al., "Implementation challenges and opportunities in beyond-5G and 6G communication," *IEEE J. Microw.*, vol. 1, no. 1, pp. 86–100, Jan. 2021, doi: 10.1109/JMW.2020.3034648.

[4] H. Tataria et al., "6G wireless systems: Vision, requirements, challenges, insights, and opportunities," *Proc. IEEE*, vol. 109, no. 7, pp. 1166–1199, Jul. 2021, doi: 10.1109/JPROC.2021.3061701.

[5] T. Kawanishi et al., "Terahertz and photonics seamless short-distance links for future mobile networks," *Radio Sci.*, vol. 56, 2021, Art. no. e2020RS007156, doi: 10.1029/2020RS007156.

[6] G. Xu and M. Skorobogatiy, "Wired THz communications," *J. Infrared, Millimeter, Terahertz Waves*, vol. 43, pp. 728–778, 2022, doi: https://doi.org/10.1007/s10762-022-00879-x.

[7] Z. Wu, M. Liang, W.-R. Ng, M. Gehm, and H. Xin, "Terahertz horn antenna based on hollow-core electromagnetic crystal (EMXT) structure," *IEEE Trans. Antennas Propag.*, vol. 60, no. 12, pp. 5557–5563, Dec. 2012, doi: 10.1109/TAP.2012.2211318.

[8] T. Tajima, H.-J. Song, K. Ajito, M. Yaita, and N. Kukutsu, "300-GHz step-profiled corrugated horn antennas integrated in LTCC," *IEEE Trans. Antennas Propag.*, vol. 62, no. 11, pp. 5437–5444, Nov. 2014, doi: 10.1109/TAP.2014.2350520.

[9] B. Zhang et al., "Metallic 3-D printed antennas for millimeter- and submillimeter wave applications," *IEEE Trans. THz Sci. Technol.*, vol. 6, no. 4, pp. 592–600, Jul. 2016, doi: 10.1109/TTHZ.2016.2562508.

[10] J. Xu, Z. N. Chen, X. Qing, and W. Hong, "140-GHz TE20-mode dielectric-loaded SIW slot antenna array in LTCC," *IEEE Trans. Antennas Propag.*, vol. 61, no. 4, pp. 1784–1793, Apr. 2013, doi: 10.1109/TAP.2012.2220317.

[11] D. Kim, J. Hirokawa, M. Ando, J. Takeuchi, and A. Hirata, "64×64-element and 32×32-element slot array antennas using double-layer hollow-waveguide corporate-feed in the 120 GHz band," *IEEE Trans. Antennas Propag.*, vol. 62, no. 3, pp. 1507–1512, Mar. 2014, doi: 10.1109/TAP.2013.2296318.

[12] K. Tekkouk et al., "Corporate-feed slotted waveguide array antenna in the 350-GHz band by silicon process," *IEEE Trans. Antennas Propag.*, vol. 65, no. 1, pp. 217–225, Jan. 2017, doi: 10.1109/TAP.2016.2631132.

[13] M. M. Zhou and Y. J. Cheng, "D-band high-gain circular-polarized plate array antenna," *IEEE Trans. Antennas Propag.*, vol. 66, no. 3, pp. 1280–1287, Mar. 2018, doi: 10.1109/TAP.2018.2796299.

[14] S. Atakaramians, S. Afshar V., T. M. Monro, and D. Abbott, "Terahertz dielectric waveguides," *Adv. Opt. Photon.*, vol. 5, pp. 169–215, 2013, doi: 10.1364/AOP.5.000169.

[15] Y. Torabi, G. Dadashzadeh, A. Lalbakhsh, and H. Oraizi, "High-gain and low-profile dielectric-image-line leaky-wave-antenna for wide-angle beam scanning at sub-THz frequencies," *Opt. Laser Technol.*, vol. 150, 2022, Art. no. 107968, doi: 10.1016/j.optlastec.2022.107968.

[16] V. B. Bui, Y. Inoue, and H. Moritake, "NRD waveguide-type terahertz phase shifter using nematic liquid crystal," *Jpn. J. Appl. Phys.*, vol. 58, 2019, Art. no. 022001, doi: 10.7567/1347-4065/aaf282.

[17] C.-M. Liu, L.-P. Carignan, S. Xiao, Y. He, and K. Wu, "Substrate-integrated hybrid metallo-dielectric waveguide architecture for millimeter-wave and terahertz applications," *IEEE Trans. Microw. Theory Tech.*, vol. 71, no. 9, pp. 3958–3967, Sep. 2023, doi: 10.1109/TMTT.2023.3249047.

[18] R. A. S. D. Koala, M. Fujita, and T. Nagatsuma, "Nanophotonics-inspired all-silicon waveguide platforms for terahertz integrated systems," *Nanophotonics*, vol. 11, pp. 1741–1759, 2022, doi: 10.1515/nanoph-2021-0673.

[19] A. Kumar et al., "Terahertz topological photonic integrated circuits for 6G and beyond: A perspective," *J. Appl. Phys.*, vol. 132, 2022, Art. no. 140901, doi: 10.1063/5.0099423.

[20] D. Headland, M. Fujita, G. Carpintero, T. Nagatsuma, and W. Withayachumnankul, "Terahertz integration platforms using substrateless all-silicon microstructures," *APL Photon.*, vol. 8, 2023, Art. no. 091101, doi: 10.1063/5.0158350.

[21] J. Liang, W. Gao, H. Lees, and W. Withayachumnankul, "All-silicon terahertz planar horn antenna," *IEEE Antennas Wireless Propag. Lett.*, vol. 20, no. 11, pp. 2181–2185, Nov. 2021, doi: 10.1109/LAWP.2021.3094310.

[22] T. Ishi, J. Fujikata, K. Makita, T. Baba, and K. Ohashi, "Si nano-photodiode with a surface plasmon antenna," *Jpn. J. Appl. Phys.*, vol. 44, pp. L364–L366, 2005, doi: 10.1143/JJAP.44.L364.

[23] Z. Han and S. I. Bozhevolnyi, "Radiation guiding with surface plasmon polaritons," *Rep. Prog. Phys.*, vol. 76, 2013, Art. no. 016402, doi: 10.1088/0034-4885/76/1/016402.

[24] J. Lin et al., "Polarization-controlled tunable directional coupling of surface plasmon polaritons," *Science*, vol. 340, pp. 331–334, 2013, doi: 10.1126/science.1233746.

[25] W. Sun, Q. He, S. Sun, and L. Zhou, "High-efficiency surface plasmon meta-couplers: Concept and microwave-regime realizations," *Light Sci. Appl.*, vol. 5, 2016, Art. no. e16003, doi: 10.1038/lsa.2016.3.

[26] T. Okatani, S. Sekiguchi, K. Hane, and Y. Kanamori, "Surface-plasmon-coupled optical force sensors based on metal–insulator–metal metamaterials with movable air gap," *Sci. Rep.*, vol. 10, 2020, Art. no. 14807, doi: 10.1038/s41598-020-71825-x.

[27] M. Beruete et al., "Very low-profile 'Bull's Eye' feeder antenna," *IEEE Antennas Wireless Propag. Lett.*, vol. 4, pp. 365–368, 2005, doi: 10.1109/LAWP.2005.851104.

[28] K. Ishihara et al., "Terahertz near-field imaging using enhanced transmission through a single subwavelength aperture," *Jpn. J. Appl. Phys.*, vol. 44, pp. L929–L931, 2005, doi: 10.1143/JJAP.44.L929.

[29] K. Ishihara et al., "Terahertz wave enhanced transmission through a single subwavelength aperture with periodic surface structures," *Jpn. J. Appl. Phys.*, vol. 44, pp. L1005–L1007, 2005, doi: 10.1143/JJAP.44.L1005.

[30] K. Ishihara et al., "Terahertz-wave near-field imaging with subwavelength resolution using surface-wave-assisted bow-tie aperture," *Appl. Phys. Lett.*, vol. 89, 2006, Art. no. 201120, doi: 10.1063/1.2387984.

[31] H. Aouani et al., "Plasmonic antennas for directional sorting of fluorescence emission," *Nano Lett.*, vol. 11, pp. 2400–2406, 2011, doi: 10.1021/nl200772d.

[32] J. H. Park, S. E. Han, P. Nagpal, and D. J. Norris, "Observation of thermal beaming from tungsten and molybdenum bull's eyes," *ACS Photon.*, vol. 3, pp. 494–500, 2016, doi: 10.1021/acsphotonics.6b00022.

[33] U. Beaskoetxea, S. Maci, M. Navarro-Cía, and M. Beruete, "3-D-printed 96 GHz bull's-eye antenna with off-axis beaming," *IEEE Trans. Antennas Propag.*, vol. 65, no. 1, pp. 17–25, Jan. 2017, doi: 10.1109/TAP.2016.2628322.

[34] Y. Takida et al., "Extraordinary transmission of bull's eye structure observed by up-conversion-based THz-wave frequency-domain spectroscopy," in *Proc. 47th Int. Conf. Infrared, Millimeter Terahertz Waves*, 2022, pp. 1–2, doi: 10.1109/IRMMW-THz50927.2022.9895791.

[35] X. Shen and T. J. Cui, "Ultrathin plasmonic metamaterial for spoof localized surface plasmons," *Laser Photon. Rev.*, vol. 8, pp. 137–145, 2014, doi: 10.1002/lpor.201300144.
[36] J. Y. Yin et al., "Frequency-controlled broad-angle beam scanning of patch array fed by spoof surface plasmon polaritons," *IEEE Trans. Antennas Propag.*, vol. 64, no. 12, pp. 5181–5189, Dec. 2016, doi: 10.1109/TAP.2016.2623663.
[37] F. J. Garcia-Vidal et al., "Spoof surface plasmon photonics," *Rev. Mod. Phys.*, vol. 94, 2022, Art. no. 025004, doi: 10.1103/RevModPhys.94.025004.
[38] S. Carretero-Palacios et al., "Mechanisms for extraordinary optical transmission through bull's eye structures," *Opt. Exp.*, vol. 19, pp. 10429–10442, 2011, doi: 10.1364/OE.19.010429.
[39] A. A. Oliner, "Radiating periodic structures: Analysis in terms of k versus β diagrams," in *Short Course on Microwave Field and Network Techniques*. Brooklyn, NY, USA: Polytechnic Institute of Brooklyn, 1963.
[40] D. R. Jackson, A. A. Oliner, T. Zhao, and J. T. Williams, "Beaming of light at broadside through a subwavelength hole: Leaky wave model and open stopband effect," *Radio Sci.*, vol. 40, 2005, Art. no. RS6S10, doi: 10.1029/2004RS003226.
[41] D. R. Jackson, J. Chen, R. Qiang, F. Capolino, and A. A. Oliner, "The role of leaky plasmon waves in the directive beaming of light through a subwavelength aperture," *Opt. Exp.*, vol. 16, pp. 21271–21281, 2008, doi: 10.1364/OE.16.021271.
[42] J. Petersen, J. Volz, and A. Rauschenbeutel, "Chiral nanophotonic waveguide interface based on spin-orbit interaction of light," *Science*, vol. 346, pp. 67–71, 2014, doi: 10.1126/science.1257671.
[43] M. F. Picardi, A. V. Zayats, and F. J. Rodríguez-Fortuño, "Janus and Huygens dipoles: Near-field directionality beyond spin-momentum locking," *Phys. Rev. Lett.*, vol. 120, 2018, Art. no. 117402, doi: 10.1103/PhysRevLett.120.117402.
[44] S. Ohno, Y. Tokizane, J. Shikata, and H. Minamide, "Phase and direction control of a terahertz wave propagating in a waveguide coupled with a bull's-eye structure," *URSI Radio Sci. Lett.*, vol. 2, pp. 1–4, 2020, doi: 10.46620/20-0030.
[45] D. Headland, W. Withayachumnankul, X. Yu, M. Fujita, and T. Nagatsuma, "Unclad microphotonics for terahertz waveguides and systems," *J. Lightw. Technol.*, vol. 38, no. 24, pp. 6853–6862, Dec. 2020, doi: 10.1109/JLT.2020.3021681.
[46] R. Koala et al., "Ultra-low-loss and broadband all-silicon dielectric waveguides for WR-1 band (0.75–1.1 THz) modules," *Photonics*, vol. 9, 2022, Art. no. 515, doi: 10.3390/photonics9080515.
[47] C. Schwarzbach and E. Haber, "Finite element based inversion for time-harmonic electromagnetic problems," *Geophys. J. Int.*, vol. 193, pp. 615–634, 2013, doi: 10.1093/gji/ggt006.
[48] T. Fukazawa, T. Hirano, F. Ohno, and T. Baba, "Low loss intersection of Si photonic wire waveguides," *Jpn. J. Appl. Phys.*, vol. 43, pp. 646–647, 2004, doi: 10.1143/JJAP.43.646.
[49] K. Nawata, Y. Tokizane, Y. Takida, and H. Minamide, "Tunable backward terahertz-wave parametric oscillation," *Sci. Rep.*, vol. 9, 2019, Art. no. 726, doi: 10.1038/s41598-018-37068-7.
[50] Y. Takida, K. Nawata, and H. Minamide, "Injection-seeded backward terahertz-wave parametric oscillator," *APL Photon.*, vol. 5, 2020, Art. no. 061301, doi: 10.1063/5.0007306.
[51] J. E. Muldera, K. Nawata, Y. Takida, D. Yadav, and H. Minamide, "Tunable backward terahertz-wave parametric oscillator centered at a high frequency of 0.87 THz with injection seeding," *Opt. Exp.*, vol. 31, pp. 23966–23973, 2023, doi: 10.1364/OE.494232.
[52] Y. Suzaki and A. Tachibana, "Measurement of the μm sized radius of Gaussian laser beam using the scanning knife-edge," *Appl. Opt.*, vol. 14, pp. 2809–2810, 1975, doi: 10.1364/AO.14.002809.
[53] N. Oshima, K. Hashimoto, S. Suzuki, and M. Asada, "Terahertz wireless data transmission with frequency and polarization division multiplexing using resonant-tunneling-diode oscillators," *IEEE Trans. THz Sci. Technol.*, vol. 7, no. 5, pp. 593–598, Sep. 2017, doi: 10.1109/TTHZ.2017.2720470.
[54] M. Gustafsson and M. Capek, "Maximum gain, effective area, and directivity," *IEEE Trans. Antennas Propag.*, vol. 67, no. 8, pp. 5282–5293, Aug. 2019, doi: 10.1109/TAP.2019.2916760.
[55] M. Yang et al., "Split bull's eye antenna for high-speed photodetector in the range of visible to mid-infrared," *IEEE Photon. Technol. Lett.*, vol. 28, no. 11, pp. 1177–1180, Nov. 2016, doi: 10.1109/LPT.2016.2535219.
[56] M. Navarro-Cía, U. Beaskoetxea, J. Teniente, and M. Beruete, "Low-sidelobe-level millimeter-wave asymmetric bull's eye antenna with minimal profile feeding," *IEEE Antennas Wireless Propag. Lett.*, vol. 23, no. 1, pp. 209–213, Jan. 2024, doi: 10.1109/LAWP.2023.3321411.
[57] T. Okatani, Y. Sato, K. Imai, K. Hane, and Y. Kanamori, "Improvement of silicon microdisk resonators with movable waveguides by hydrogen annealing treatment," *J. Vac. Sci. Technol. B*, vol. 39, 2021, Art. no. 030602, doi: 10.1116/6.0000971.
[58] S. Freer et al., "Loss characteristics of terahertz surface waves on laser micromachined textured metals," *IEEE Trans. THz Sci. Technol.*, vol. 14, no. 2, pp. 283–292, Mar. 2024, doi: 10.1109/TTHZ.2024.3358738.
[59] E. Carrasco, M. Tamagnone, and J. Perruisseau-Carrier, "Tunable graphene reflective cells for THz reflectarrays and generalized law of reflection," *Appl. Phys. Lett.*, vol. 102, 2013, Art. no. 104103, doi: 10.1063/1.4795787.
[60] X. J. Fu, F. Yang, C. X. Liu, X. J. Wu, and T. J. Cui, "Terahertz beam steering technologies: From phased arrays to field-programmable metasurfaces," *Adv. Opt. Mater.*, vol. 8, 2020, Art. no. 1900628, doi: 10.1002/adom.201900628.
[61] D. Yang et al., "Programmable VO_2 metasurface for terahertz wave beam steering," *iScience*, vol. 25, 2022, Art. no. 104824, doi: 10.1016/j.isci.2022.104824.
[62] Y. Huang, T. Okatani, N. Inomata, and Y. Kanamori, "A reconfigurable ladder-shaped THz metamaterial integrated with a microelectromechanical cantilever array," *Appl. Phys. Lett.*, vol. 122, 2023, Art. no. 051705, doi: 10.1063/5.0124601.
[63] Y. Huang, T. Okatani, N. Inomata, and Y. Kanamori, "Reconfigurable THz metamaterial based on microelectromechanical cantilever switches with a dimpled tip," *Opt. Exp.*, vol. 31, pp. 29744–29754, 2023, doi: 10.1364/OE.497514.
[64] Y. Fu et al., "Two-dimensional terahertz beam manipulations based on liquid-crystal-assisted programmable metasurface," *Appl. Phys. Lett.*, vol. 123, 2023, Art. no. 111703, doi: 10.1063/5.0167812.
[65] Y. Monnai, D. Jahn, W. Withayachumnankul, M. Koch, and H. Shinoda, "Terahertz plasmonic Bessel beamformer," *Appl. Phys. Lett.*, vol. 106, 2015, Art. no. 021101, doi: 10.1063/1.4905445.
[66] K. Chiba, T. Okatani, N. Inomata, and Y. Kanamori, "Micro-fabricated Si subwavelength grating for frequency-domain THz beam steering covering the 0.3–0.5 THz frequency band," *Opt. Exp.*, vol. 31, pp. 27147–27160, 2023, doi: 10.1364/OE.492942.

Taiyu Okatani received the B.Eng. M.I.S.T., and Ph.D. degrees in information science and technology from The University of Tokyo, Tokyo, Japan, in 2015, 2017, and 2020, respectively.

Since 2020, he has been an Assistant Professor with the Department of Robotics, Graduate School of Engineering, Tohoku University, Sendai, Japan. His research interests include robotics, microelectromechanical systems, and metamaterials.

Kaoru Imai received the B.Eng. and M.Eng. degrees from Tohoku University, Sendai, Japan, in 2020 and 2022, respectively.

From 2020 to 2022, he was a Graduate Student with the Department of Robotics, Graduate School of Engineering, Tohoku University.

Yuma Takida received the Ph.D. degree in physical electronics and informatics from Osaka City University, Osaka, Japan, in 2013.

In 2013, he joined the Tera-Photonics Research Team, RIKEN Center for Advanced Photonics, RIKEN, Saitama, Japan, as a Postdoctoral Fellow of the Japan Society for the Promotion of Science (JSPS). He is currently a Research Scientist with RIKEN. His research interests include laser-driven terahertz-wave generation and detection, and their applications.

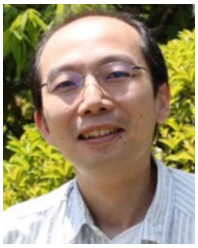

Seigo Ohno received the B.S. and Ph.D. degrees in physics from Tohoku University, Sendai, Japan, in 2001 and 2006, respectively.

In 2006, he joined Tera-photonics Laboratory, RIKEN, Saitama, Japan, as a Postdoctoral Researcher. Since 2009, he has been an Assistant Professor with Tohoku University. His research interests include nonlinear optics, terahertz light sources, and metasurfaces in the terahertz region.

Hiroaki Minamide (Member, IEEE) received the B.S. degree in communication engineering and the M.S. and Ph.D. degrees in electronic engineering from Tohoku University, Sendai, Japan, in 1993, 1996, and 1999, respectively.

In April 1999, he joined in a frontier researcher at the Photo-Dynamics Research Center, RIKEN, Saitama, Japan, and started to study on developing THz-wave source using nonlinear optical effect. He was a Deputy Team Leader from 2007 to September 2010. From October 2010, he leads Teraphotonics team of RIKEN as a Team Leader. His research interests include the development of ultra-wide tunable THz-wave in the frequency-region from sub-THz to several tens THz using organic nonlinear crystal, high-power THz-wave generation, and extremely sensitive THz-wave detection using nonlinear optics and their unique THz applications.

Dr. Minamide is a Member of Optica (formerly OSA), The Institute of Electronics, Information and Communication Engineers (IEICE), The Optical Society of Japan (OSJ), The Japan Society of Applied Physics (JSAP), and The Laser Society of Japan as a senior membership.

Yoshiaki Kanamori (Member, IEEE) received the M.Eng. and Dr.Eng. degrees from Tohoku University, Sendai, Japan, in 1998 and 2001, respectively.

From 1998 to 2001, he was a Research Fellow of the Japan Society for the Promotion of Science. From 2001 to 2007, he was a Research Associate with the Graduate School of Engineering, Tohoku University. From 2003 to 2004, he was a Postdoctoral Researcher with the Laboratory for Photonics and Nanostructures, Centre National de la Recherche Scientifique, Paris, France. From 2007 to 2019, he was an Associate Professor with the Department of Finemechanics, Tohoku University. Since 2019, he has been a Professor with the Department of Robotics, Tohoku University. From 2020 to 2022, he was the concurrent post of Director of the Micro and Nanomachining Research and Education Center (MNC), Tohoku University. In 2022, he established Metamaterials Research and Innovation Center (Meta-RIC), Tohoku University, and has been the concurrent post of Director. Since 2023, he has been a concurrent post of Professor with Green Future Creation Organization, Tohoku University. His research focuses on the the development of metamaterials, nanophotonics, microfabrications, and optical MEMS